Rapid flapping and fibre-reinforced membrane wings are key to high-performance bat flight

Lauber, M.; Weymouth, Gabriel D.; Limbert, Georges

DOI
10.1098/rsif.2023.0466

Publication date
2023

Document Version
Final published version

Published in
Journal of the Royal Society Interface

Citation (APA)
Lauber, M., Weymouth, G. D., & Limbert, G. (2023). Rapid flapping and fibre-reinforced membrane wings are key to high-performance bat flight. *Journal of the Royal Society Interface*, *20*(208), Article 20230466. https://doi.org/10.1098/rsif.2023.0466

INTERFACE

royalsocietypublishing.org/journal/rsif

Research

Cite this article: Lauber M, Weymouth GD, Limbert G. 2023 Rapid flapping and fibre-reinforced membrane wings are key to high-performance bat flight. *J. R. Soc. Interface* **20**: 20230466.
https://doi.org/10.1098/rsif.2023.0466

Received: 9 August 2023
Accepted: 20 October 2023

Subject Category:
Life Sciences–Physics interface

Subject Areas:
biomechanics

Keywords:
bat flight, simulations, fluid–structure, membrane, fibres

Author for correspondence:
Marin Lauber
e-mail: M.Lauber@tudelft.nl

Electronic supplementary material is available online at https://doi.org/10.6084/m9.figshare.c.6916153.

THE ROYAL SOCIETY PUBLISHING

Rapid flapping and fibre-reinforced membrane wings are key to high-performance bat flight

Marin Lauber[1,2], Gabriel D. Weymouth[2] and Georges Limbert[1,3]

[1]Faculty of Engineering and Physical Sciences, University of Southampton, Southampton, UK
[2]Faculty of Mechanical Maritime and Materials Engineering (3mE), Delft University of Technology, Delft, The Netherlands
[3]Department of Human Biology, Faculty of Health Sciences, University of Cape Town, Cape Town, South Africa

ML, 0000-0003-2191-9318; GDW, 0000-0001-5080-5016; GL, 0000-0002-4268-6106

Bats fly using significantly different wing motions from other fliers, stemming from the complex interplay of their membrane wings' motion and structural properties. Biological studies show that many bats fly at Strouhal numbers, the ratio of flapping to flight speed, 50–150% above the range typically associated with optimal locomotion. We use high-resolution fluid–structure interaction simulations of a bat wing to independently study the role of kinematics and material/structural properties in aerodynamic performance and show that peak propulsive and lift efficiencies for a bat-like wing motion require flapping 66% faster than for a symmetric motion, agreeing with the increased flapping frequency observed in zoological studies. In addition, we find that reduced membrane stiffness is associated with improved propulsive efficiency until the membrane flutters, but that incorporating microstructural anisotropy arising from biological fibre reinforcement enables a tenfold reduction of the flutter energy while maintaining high aerodynamic efficiency. Our results indicate that animals with specialized flapping motions may have correspondingly specialized flapping speeds, in contrast to arguments for a universally efficient Strouhal range. Additionally, our study demonstrates the significant role that the microstructural constitutive properties of the membrane wing of a bat can have in its propulsive performance.

1. Introduction

Bats are amazing fliers able to perform powered flight using membrane wings which endow them with exceptional manoeuvring capabilities [1]. Understanding the complex mechanical interplay of their membrane wing and flight kinematics is key to unravelling fundamental questions in evolutionary biology and to engineering of biologically inspired flying vehicles.

Numerous studies have investigated the kinematics of bats in forward flight [2–7] and provided details of its unique features. Bats fly using a power stoke where the aerodynamic forces are mainly produced during the downstroke while the upstroke is comparatively far less active and can even be feathered [8,9]. The downstroke starts with the wing moving ventrally and anteriorly along the stroke plane (figure 1*a*). An essential parameter of bat (and animal) flight is the angle of the stroke plane relative to the horizontal, which tends to increase with flight speed [1]. Wing extension is also a key influencing parameter of bat flight; it is maximal during the downstroke to enhance aerodynamic force production [12] while it is minimal during the upstroke to reduce power expenditure [13]. An aspect that differentiates bat flight from that of other flying animals is their wing's weight, representing up to 20% of their total weight [14], which influences the power requirements of bats. While these studies provide excellent observation of bat flight, they cannot

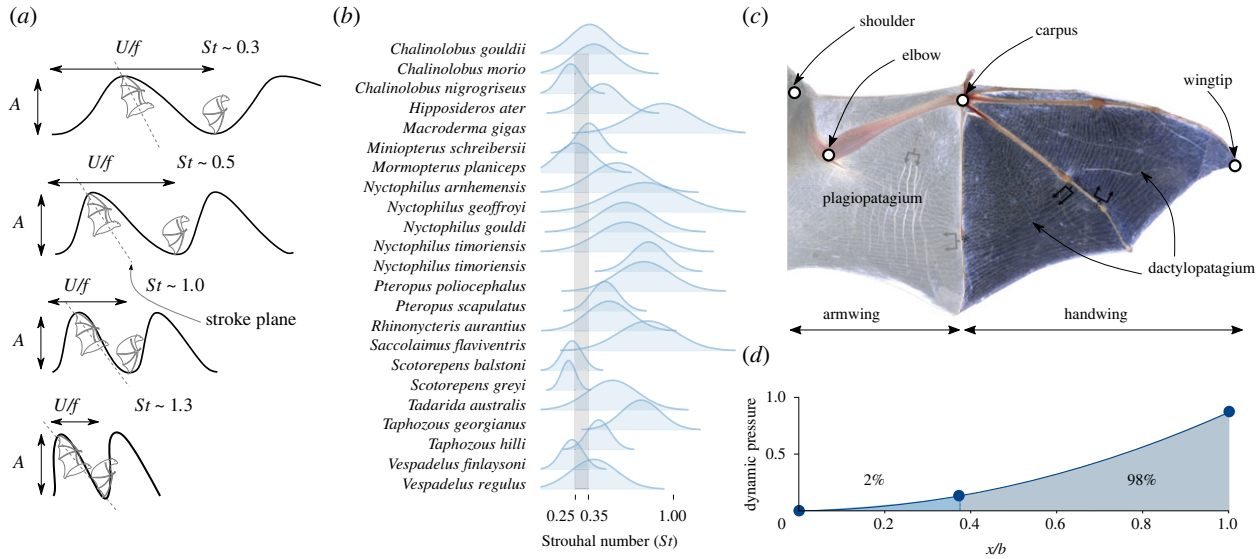

Figure 1. Schematic of (*a*) the Strouhal number of a bat wing showing the wingtip trajectory (black line) and the stroke plane (dashed grey line); adapted from Swartz & Konow [1]. (*b*) Strouhal number envelope for several bat species from the data provided in [10]. The normal distribution is drawn with a variance where the min–max envelope corresponds to $\pm 3\sigma$ (99.7% confidence interval), and the mean uses the mean Strouhal number from the data. The grey shaded area represents the typical Strouhal range of $0.25 < St < 0.35$. (*c*) Macroscopic structure of a bat wing membrane. Asterisks indicate the array of nearly homogeneous, approximately spanwise-oriented *elastin* fibres; dagger indicates the chordwise-oriented *musclesin* in the armwing; adapted from Swartz & Konow [11]. (*d*) Distribution of relative pressure due to dynamic motion along the wing's span computed from experimental measurements [4].

isolate the essential aspects of kinematics and their influence on flight efficiency. Additionally, reported flapping frequencies across numerous bat species can vary by as much as 50% compared to those of morphologically similar birds, at equivalent flight speed and flapping amplitude [10,15]. We compile the experimental measurements of Bullen & McKenzie [10] (see electronic supplementary material, Appendix table S1) in terms of the Strouhal number *St*:

$$St = \frac{fA}{U} \sim \frac{\text{flapping speed}}{\text{flight speed}}, \tag{1.1}$$

with f the flapping frequency, U the forward velocity of the swimmer/flyer and A the peak-to-peak flapping amplitude; see figure 1*a*. Animal flight or swimming typically occurs in a narrow range of Strouhal numbers, $0.25 < St < 0.35$, and this narrow band is linked to optimal locomotion in terms of propulsive efficiency [16] associated with the most unstable mode of the wake. However, figure 1*b* shows that many bats fly at Strouhal numbers significantly higher than this, and we find that the motion amplitude is a good measure of wake width, see electronic supplementary material, Appendix figure S1, meaning our use of A in defining *St* is consistent. As such, the anomaly in the Strouhal number indicates that bat flight is an outlier compared to other flapping animals.

In addition to bat flight's uniquely high Strouhal number, bat wing material properties are also unique, arising from a complex arrangement of various types of elastic fibres and muscles. Typical membrane thicknesses range between 130 and 300 µm, making them extremely thin compared to other mammals' skin [17]. Fibre assemblies in the *plagiopatagium* and the *dactylopatagium* form an orthogonal net [17], with the fibres approaching the digits at 90° to the digit long axis. These fibre arrangements are volumetrically dominated by spanwise *elastin* fibres featuring a high degree of elastic recoil, while the much stiffer *collagen* fibres are present in much smaller proportions. Within this orthogonal fibre network, there is a significant stiffness ratio between the spanwise and chordwise mechanical properties [18]; see figure 2*c*. The high level of mechanical anisotropy of the wing results from pre-stretched spanwise elastin fibres embedded in a matrix with randomly oriented collagen fibres [11]. At rest, the pre-stretched elastin fibres induce buckling of the supporting matrix. Under tension, the much stiffer matrix and collagen fibres increase spanwise stiffness once the elastin fibres have been stretched past the unwrinkled configuration of the membrane. While it has been hypothesized that this fibrous net improves flight efficiency [19,20], this has not been verified nor quantified with parametric studies rooted in continuum mechanics of both fluid and solid media.

Experimental studies of bat flight are limited in the amount of information that can be simultaneously collected about the structural and material properties of the wing, and motion of the bat during flight. Therefore, these studies cannot segregate the respective role of particular structural elements of the membrane/wing composition or that of flight kinematics in the bat's performance. Similarly, previous numerical simulations rely either on marker measurements, *fixed* and *discrete* by definition, and one-way fluid–structure interaction coupling [12,21], or on overly simplistic kinematics and constitutive laws for membrane skin [22,23]. In the first case, these numerical studies inherit the experimental study's *fixed* set of parameters by design, thus preventing any further wider parametric studies, and in the second case, the respective influence of the microstructural constitutive parameters and motions of the wing membrane, and their interplay, are not captured because of the low fidelity of the kinematics and material law used. The research presented here uses fully coupled fluid–structure simulations to perform the first controlled study of bat performance using realistic parametric models of the bat flight motion in concert with state-of-the-art microstructurally based constitutive

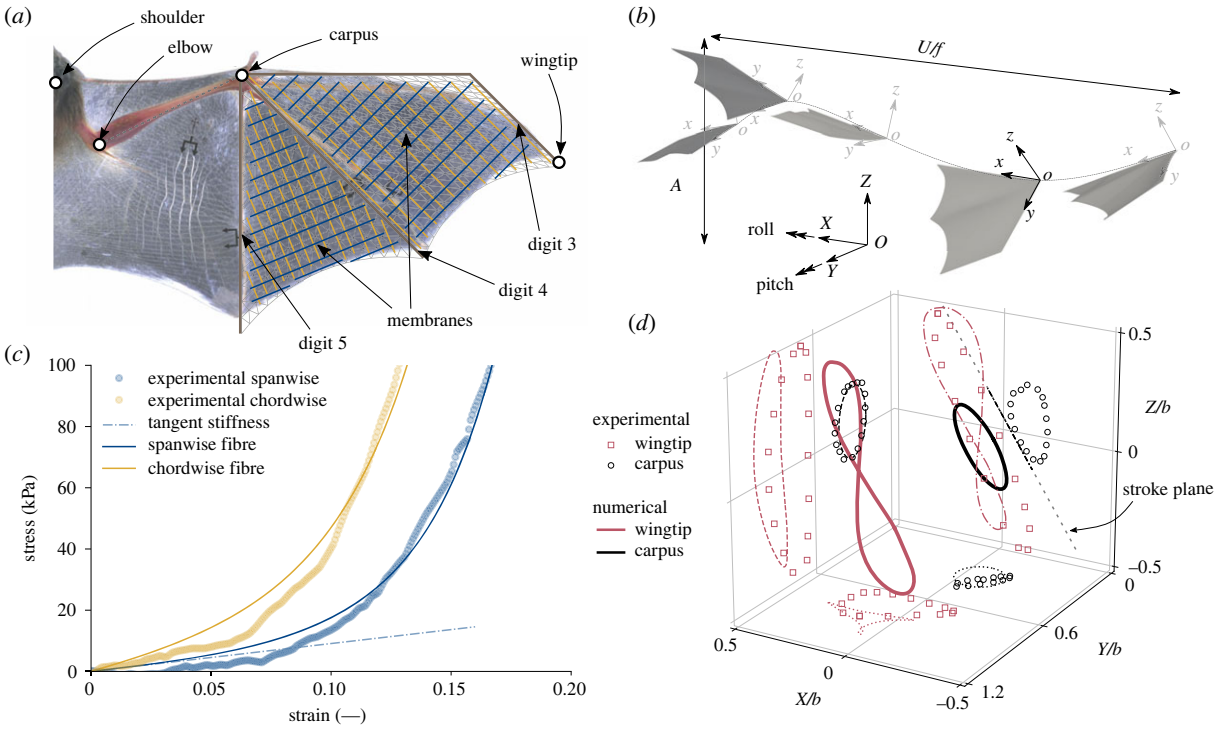

Figure 2. Schematic of the kinematic and geometrical model of the bat wing. (*a*) Coarse representation of the finite-element model of the handwing used for the numerical simulations with the fibre family direction vector. (*b*) Cartesian (*OXYZ*) and carpus (*oxyz*) coordinate system. The carpus coordinate system is convected with the wing following the dashed path. Pitch and roll are rotations around the *Y*-axis and *X*-axis, respectively. The Strouhal number, $St = A/(U/f)$, is depicted for kinematics at $St = 0.5$. (*c*) Constitutive curves for the fibre-reinforced membrane under biaxial loading showing the membrane's nonlinear behaviour and the tangent stiffness modulus for calibrating the mechanical properties. The constitutive curves correspond to the two fibre families in (*a*). The tangent stiffness modulus shows a response equivalent to linear isotropic material. (*d*) Trajectory of the wingtip and carpus in a three-dimensional space (thick lines) with projections onto the three planes (various discontinuous lines) for a Strouhal number $St = 0.5$ compared to experimental measurements (markers) of Wolf *et al.* [4]. The stroke plane is represented by the dashed grey line. The experimental Strouhal number is estimated to be $St \sim 0.5$.

model of the wing membrane valid for arbitrary (i.e. *finite*) deformation. Computational studies are indispensable for these complex systems that are intractable analytically [24]. By investigating the flapping Strouhal number and membrane reinforcement independently, we determine their direct influence on the flow field and wing deformations and ultimately explain the influence of these unique features on bat flight performance.

2. Results

2.1. Parametric modelling approach

Our geometrical model of the bat wing consists of the three distal digits (3, 4 and 5) and the membranes that make up the handwing; see figure 2*a*. The handwing experiences 98% of the dynamic load during a cycle (figure 1*d*) and significantly contributes to both lift and thrust. Previous quasi-steady models of bat flight [14] estimate that thrust is produced mostly by the handwing while lift contributions are shared equally between the hand- and armwing. However, the armwing relies on complex muscle activity to generate lift by modulating the camber of the (*plagiopatagium*) membrane [20], while the handwing relies on the large apparent velocity induced by the motion and camber modulation via folding of the digits. Attempting to actively control the time-dependent muscle and digit activity would add significant complexity and uncertainty to our geometric and kinematic model of the wing. While omitting part of the biological system such as the body and secondary lifting surfaces certainly introduces errors, focusing on the dominant contributor to the propulsive force has been used in many successful numerical studies [25,26]. We, therefore, limit the current study to the handwing with inactivated digits and focus on the dynamic thrust and lift production and passive deformation of that structure. The flight kinematics are imposed on our geometrical model through the *carpus*; see figure 2*a*.

Bats use complex pitching, folding and active camber control of their wing during the cycle to modulate the thrust/lift generation. Lift is mainly produced in the downstroke, and the upstroke has a minor contribution to the cycle-averaged values, while thrust is produced throughout the cycle [12]. Mimicking the loading applied during the downstroke and upstroke is critical to achieving realistic performance estimates (see electronic supplementary material, Appendix figure S2), but modelling the folding of the wing during the upstroke is extremely complex. To provide simplified yet realistic kinematics, we prescribe a variable pitch to our model based on an effective angle of attack approach [27,28]. This is an approximate method used to quickly estimate appropriate pitch kinematics, after which the full fluid–structure interaction solver is used to determine the resulting flight performance. However, this simple approach captures bat wing motion accurately when compared to actual wing motion [4]; see figure 2*d*. The complete kinematics, their calibration, and the procedure used to obtain the pitch profiles are presented in the Methods section.

We use our fully coupled fluid–structure interaction solver, presented in [29,30], to perform numerical simulations

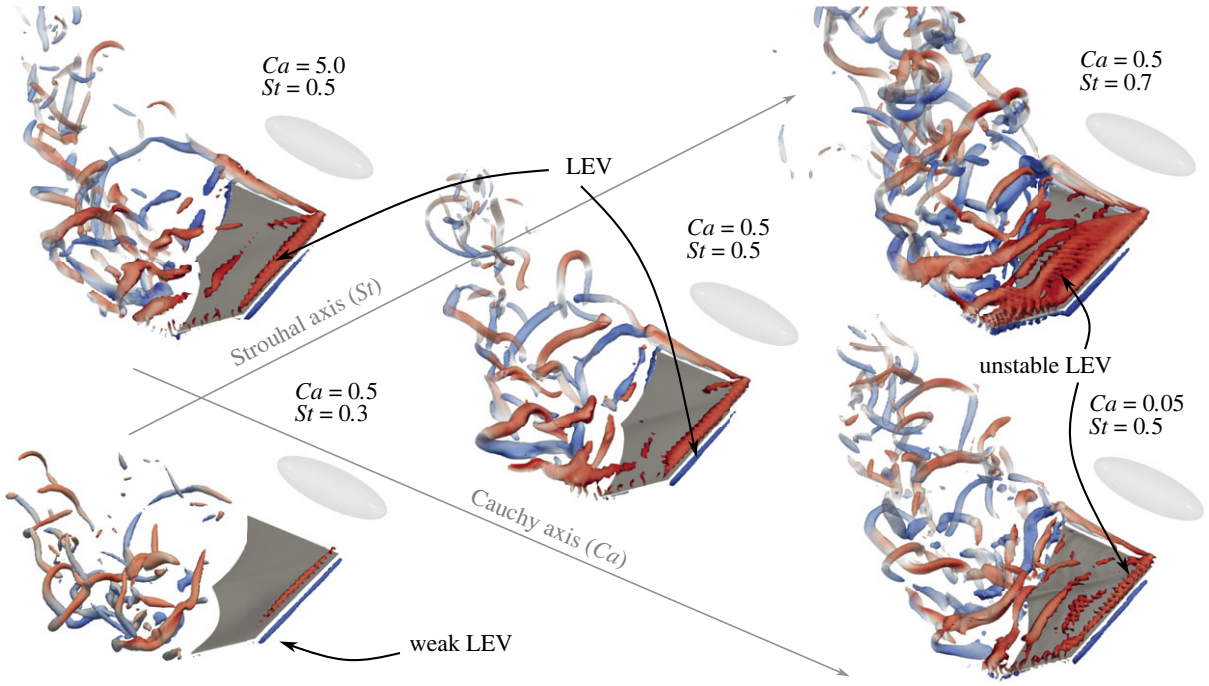

Figure 3. Vortex structures in the wake of the bat represented by isosurfaces of $\lambda_2(b/U)^2 = -5 \times 10^{-6}$ coloured by spanwise vorticity $\omega_y(b/U) \pm 50$ at a selected time during the downstroke. Three different Strouhal numbers at a fixed Cauchy number $Ca = 0.5$ are represented on the bottom-left to top-right axis and three different membrane Cauchy numbers at a fixed Strouhal number $St = 0.5$ are represented on the top-left to bottom-right axis. The bat's body (absent from flow computation) is represented by the opaque ellipsoid, which is not necessarily scaled to the wing. Arrows identify leading edge vortex (LEV).

of our parametric geometric and kinematic model of a bat wing; see figure 2*a* and the Methods section for more details. In addition to Strouhal number St, three non-dimensional parameters govern the coupled problem: the Reynolds number, $Re = Ub/\nu_a$, the mass ratio, $M_\rho = \rho_s h/\rho_a b$, and the Cauchy number,

$$Ca = \frac{Eh}{\rho_a U_{\text{ref}}^2 b} \sim \frac{\text{membrane stiffness}}{\text{dynamic pressure}}, \tag{2.1}$$

where ν_a, b, E and h are the kinematic viscosity of air, the bat's half-span, Young's modulus and the membrane thickness, respectively. ρ_s and ρ_a are the membrane and air density, respectively. The velocity scale, U_{ref}, is the maximum apparent velocity during the cycle $U_{\text{ref}}^2/U^2 = 1 + (\pi St)^2$. This Ca scaling ensures that the impact of Strouhal number on the relative stiffness of the wing is accounted for, allowing us to study the relative speed and stiffness effects independently. Using typical bat wing membrane density [17], the mass ratio is set to $M_\rho = 0.589$. The full viscous flow equations are solved, and assuming a standard cruising speed and a wingspan of bats, the Reynolds number is set to $Re = 10^4$. We study the Strouhal range $St = 0.3$–0.7 based on figure 1*b*. A simple estimate of bat Cauchy number assuming a membrane wing with a thickness of 150 µm [17] and a wing span of 0.1 m, a reference (max. apparent) velocity of 10 m s^{-1} and a tangent stiffness modulus 0.250 GPa [18] gives $Ca \sim 0.3$, and we simulate a wide range of Ca around this estimate.

We start by presenting results for a linear isotropic elastic constitutive law to investigate the effect of the flapping speed and stiffness of the membrane wing on the aerodynamic efficiencies. We will then compare the isotropic linear elastic model to the nonlinear fibre-reinforced formulation that incorporates microstructural and loading-induced anisotropy, more closely resembling actual characteristics of the bat wing's membrane [18,31]. Idealized responses of this fibre-reinforced model are shown in figure 2*c* together with the experimental calibration data [18]. The strain energy density function of the nonlinear fibre-reinforced formulation and the method used to calibrate the material coefficients on the experimental bat membrane data are presented in the Methods section.

2.2. Flow field characterization

Figure 3 shows the vortex structures generated by the wing at three different Strouhal numbers and three different Cauchy numbers at the same time during the downstroke ($t/T = 0.78$, with T the motion period). These visualizations show that the wake is sensitive to both the Strouhal number and the Cauchy number of the membrane. The complete unsteady flow field evolution can be viewed in electronic supplementary material, video.

The Strouhal number strongly influences the vortex structures generated by the wing (bottom-left to top-right axis in figure 3), particularly on the leading edge vortex (LEV) which generates large suction forces on the wing when fully attached [32]. At low flapping speed, a very weak LEV is generated, and the structures shed from the wing's trailing edge are confined to the tip of the wing; see figure 3. Increasing the Strouhal number to $St = 0.5$ generates a stronger LEV indicating much larger force production. A further increase of the Strouhal number to $St = 0.7$ generates a large but unstable LEV which breaks down almost immediately, limiting the duration of effective force production. The tip vortex located on the inner part of the wing results from our simplification of the bat wing, where only the handwing is modelled and is thus not present in real bat flight. However, its strength is many times less than the LEV and tip vortex due to its smaller dynamic velocity (figure 1*d*) and its influence on the results is minor.

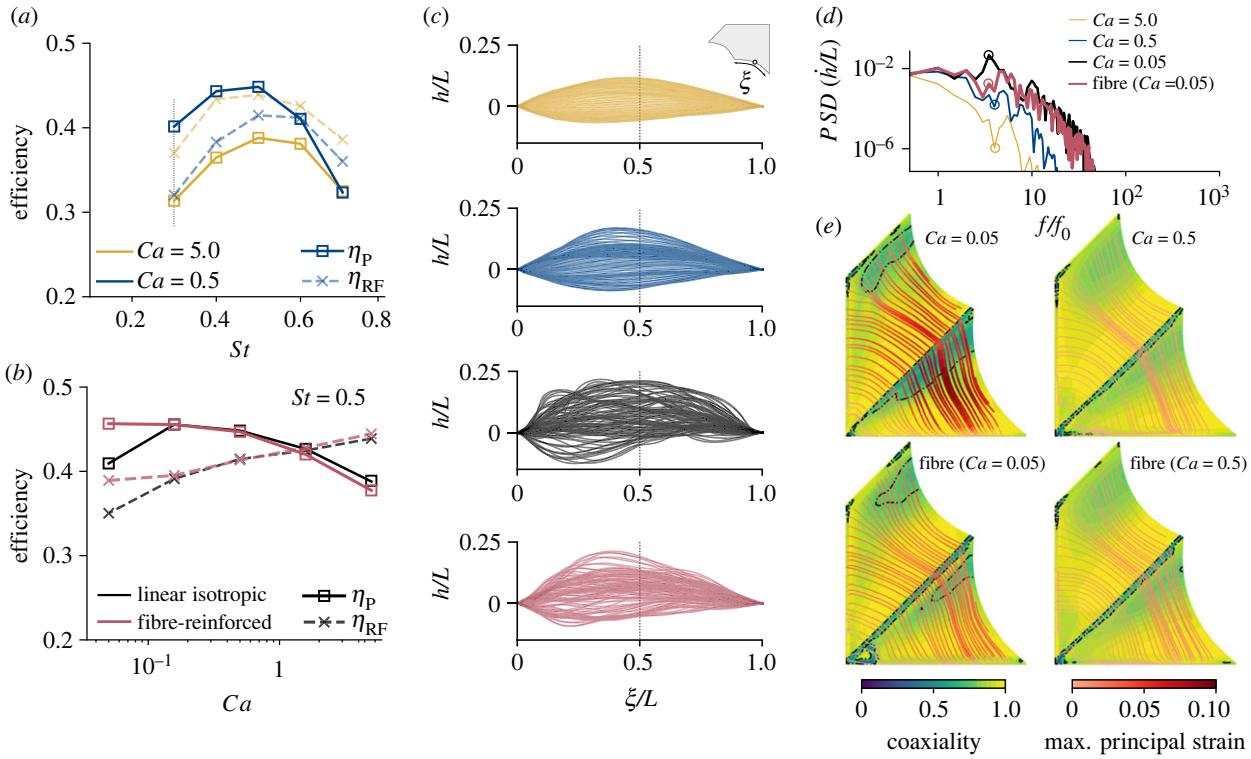

Figure 4. Propulsive and Rankine–Froude efficiency for (*a*) a linear isotropic membrane wing at various Strouhal numbers and two Cauchy numbers, and for (*b*) various Cauchy numbers and membrane material models at a fixed Strouhal number of $St = 05$. The dashed vertical line in (*a*) indicates the optimal propulsive efficiency for an identical wing model under symmetric-flapping kinematics. (*c*) Overlay of the phase-averaged vertical deformation of the trailing edge of the inner membrane at 100 times over a flapping cycle shown in the curvilinear coordinate system of the undeflected membrane trailing edge (see inset). Deflections are shown for three Cauchy numbers for the linear isotropic membrane ($Ca \in \{5.0, 0.5, 0.05\}$) and a fibre-reinforced membrane (with an equivalent $Ca = 0.05$). (*d*) Power-spectral density of the vertical velocity of the midpoint of the membrane's trailing edge against normalized frequency for the four material properties shown in (*c*). Fibre-reinforced membranes reduced the peak frequency magnitude tenfold compared to equivalent linear elastic membranes. (*e*) Streamlines of the direction of the max. principal strain ε_1 coloured by the magnitude of the max. principal strain in the membrane at $t/T = 0.78$, corresponding to the flow plot in figure 3, for two different constitutive models and membrane Cauchy numbers. Isocontours show the coaxialiality of max. principal strain with the max. principal stress σ_1. The use of fibres reduces the regions of the membrane where coaxiality is less than 0.75, indicated by the dashed contour. Contours and streamlines are shown in the undeformed configuration.

By contrast, variations in the stiffness of the membrane (top-left to bottom-right axis in figure 3) has a smaller effect on the bat's wake. For stiff membranes (i.e. high *Ca*) a LEV is generated on the wing's leading edge, but the vortices shed at the trailing edge are not spanning the entire wing span. A reduction of the membrane's stiffness (i.e smaller *Ca*) allows recovering strong vortices spanning the entire wing at the trailing edge, but a very elastic membrane generates a moderately unstable LEV. This moderately reduces the effective force production, similar to (but less extreme than) the high *St* case.

Overall, the wake is governed by the flapping speed of the wing, but within a fixed Strouhal number, the membrane's stiffness can further influence the vortex structures. We note that our simulations are able to capture some wake features observed experimentally [33], such as the span reduction during the upstroke and the transition vortex (i.e. the vortex generated during the upstroke–downstroke transition); see electronic supplementary material, video.

2.3. Effect of Strouhal number

Further quantification of the results are presented in terms of thrust, lift and power coefficient:

$$C_T = \frac{F_x}{(1/2)\rho_a S U^2}, \quad C_L = \frac{F_z}{(1/2)\rho_a S U^2}, \quad C_{\mathrm{Pow}} = \frac{\mathrm{Pow}}{(1/2)\rho_a S U^3}, \tag{2.2}$$

where measured thrust force (F_x), lift force (F_z) and the power (Pow) are calculated from the integration of pressure and viscous forces over the wing. S is the planform area of the wing, and U is the forward speed of the bat. To quantify the thrust and lift efficiency of the wing, we use the propulsive and *Rankine–Froude* (RF) [34] efficiencies, respectively:

$$\eta_{\mathrm{P}} = \frac{\overline{F_x} U}{\overline{P}} = \frac{\overline{C_T}}{\overline{C_{\mathrm{Pow}}}} \quad \text{and} \quad \eta_{\mathrm{RF}} = \frac{\overline{C_L}^{3/2}}{\overline{C_{\mathrm{Pow}}}}, \tag{2.3}$$

where an overline signifies cycle-averaged values.

The propulsive and lift efficiencies for two linear isotropic membranes with different *Ca* for a range of Strouhal numbers are presented in figure 4*a*. Regardless of membrane stiffness, both efficiencies peak at a Strouhal number $St \sim 0.5$. The reduced efficiency at high ($St = 0.7$) and low ($St = 0.3$) Strouhal numbers can be associated with the high mixing present in the wake and the small LEV present on the tip of the wing and not the entire span; see figure 3. Peak efficiencies are associated with a strong LEV, spanning the entirety of the wing span and a small amount of mixing in the wake.

The efficiency is much less sensitive to membrane stiffness than to *St*. The lift efficiency decreases slightly with the 10 times decrease in stiffness, measuring around 10% lower for $Ca = 0.5$ than for $Ca = 5.0$ across the *St* range. By contrast, the thrust efficiency increases with reduced stiffness, with a 25% improvement at $St = 0.5$ (although no change is

measured for $St > 0.6$). In terms of thrust coefficient, we find that $Ca = 0.5$ out-performs $Ca = 5.0$ for $St < 0.6$, while the opposite is true for $St > 0.6$. Lift steadily increases with St for both membrane stiffness but at a lower rate for $Ca = 0.5$, especially for $St > 0.6$. This is likely linked to a reduction of the effective angle of attack of the wing as St increases, which results in less membrane camber and less force generation for $Ca = 0.5$.

The Strouhal number corresponding to the peak in efficiency is relatively insensitive to the membrane stiffness but is strongly influenced by the kinematics. Indeed, replicating these simulations with identical geometrical and material models under *symmetric-flapping* kinematics, which are based on our bat kinematics but use symmetric pitching and flapping of the wing, showed a peak efficiency at $St \sim 0.3$; see electronic supplementary material, Appendix figure S3. While geometric factors, such as the propulsor's aspect ratio, have been known to change the optimal Strouhal number [35], our results show that keeping identical material and geometrical models but changing the motion to bat kinematics results in a 66% increase in the optimal flapping rate.

2.4. Effect of membrane stiffness and fibre reinforcement

At the peak-performance Strouhal number ($St = 0.5$), reducing membrane stiffness improves propulsive efficiency while only slightly penalizing the lift efficiency (figure 4*a*). Figure 4*b* shows the change in the efficiency at $St = 0.5$ over a 100 times reduction in membrane stiffness to quantify the performance of a highly compliant membrane. Additionally, actual bat membranes are made of complex fibre arrangements [17], and the mechanical properties deviate significantly from those of linear isotropic elastic materials; see figure 2*c*. To investigate the effect of the fibre reinforcement on bat flight, we repeat these simulations using a fibre-reinforced membrane; see the Methods section. The results are shown in figure 4*b* on top of the linear isotropic elastic membrane results. For linear isotropic membranes, the propulsive efficiency increases with reduced membrane stiffness (i.e. reduced Ca). The maximum propulsive efficiency is reached at $Ca \sim 0.1$ before abruptly dropping. Lift efficiency steadily decreases with decreased membrane stiffness, and the drop observed $Ca < 0.1$ for the propulsive efficiency is not as severe. Adding fibre reinforcements to the membranes does not significantly change the performance of stiff membranes (i.e. large Ca). However, at very low stiffness (i.e. small Ca), adding fibre reinforcements allow a 10% gain in propulsive and lift efficiencies and no drop-off. This loss in efficiencies near $Ca = 0.05$ for linear isotropic membranes corresponds to the onset of flutter of the membrane and increased vortex shedding in the wake; see figure 3. Figure 4*c* documents the flutter in terms of the phase-averaged trailing edge deflection of the membrane. Deflections are shown in the frame of reference of the undeformed membrane (see inset in figure 4*c*). The corresponding power-spectral density (PSD) of the vertical velocity of the trailing edge's midpoint also indicates flutter; see figure 4*d*. Membrane flutter introduces high-frequency oscillations of the membrane and shifts the peak frequency of the membrane above the motion frequency. This high-frequency oscillation contains ten times the energy of stiffer membranes. By introducing fibre reinforcement to the membranes, the internal response of the wing is changed (see below), and the aerodynamic efficiency is improved.

These very flexible membranes also increase the high-frequency mixing of the fluid, as measured by the *enstrophy* $\mathcal{E}$, the integral of the square-vorticity in the fluid domain. We measure a strong inverse Pearson's correlation $\rho_{\mathcal{E},\eta} = -0.976$ with p-value of 0.00436 between the mean enstrophy during a cycle and the propulsive efficiency at $St = 0.5$; see electronic supplementary material, Appendix figure S4. This is because excessive fluid mixing requires significant power input from the wing without a large gain in force production. The flutter induced by a very flexible membrane generates the most enstrophy in the bat's wake, explaining the poor aerodynamic efficiency in figure 4*b* at very low Ca, whereas fibre-reinforced membrane limits the flutter and thus the mixing in the wake, which allows maintaining high aerodynamic efficiencies.

We document the internal response of the membrane in terms of the direction and magnitude of the principal strain in figure 4*e*. When the membrane has a low linear stiffness ($Ca = 0.05$), fibre reinforcements greatly reduce the maximum strain in the membrane from 9.4% to 4.1% due to the loading-induced nonlinear stiffening of the fibre at high strain; see figure 2*c*. This effect is similar to an increase in stiffness of a linear isotropic membrane without requiring a thicker membrane, which explains the extremely low thickness of the bat's membrane. This loading-induced stiffening does not activate for the $Ca = 0.5$ membrane because the strains are too low. Figure 4*e* also shows that fibre-reinforcing the $Ca = 0.05$ membrane also reduces the region of low coaxiality of the principal stress and strain in the membrane by 60%. Coaxiality of the stress and strain tensors corresponds to a state of deformation in which the principal directions of both tensors are aligned [36]. This metric indicates the state of isotropy of stress and strain that biological tissues appear to maximize through internal microstructure evolution since it minimizes their strain energy [37,38]. This principle of energy minimization is commonly considered a fundamental axiom in Nature.

3. Conclusion

In this paper, we performed fully coupled computational fluid–structure interaction simulations of a bat wing with fully adjustable parametric kinematics and material model. The parametric models are simplified compared to real-life bat kinematics and wings, but capture the essential nonlinear aspects of bat flight and mechanical membrane behaviour (figure 2*c*,*d*), making these results relevant to actual bat flight. These models allow us to separately investigate the effects of the Strouhal number and membrane compliance on the flight performance of bats, as well as giving detailed insights into the structural response of the wing's membrane. First, we show that bats operate at a Strouhal number corresponding to a peak in both propulsive and lift efficiencies. This peak occurs near Strouhal number $St \sim 0.5$, which agrees well with the mean Strouhal number of actual bats; see figure 1*a*. This peak is also well above the range commonly associated with optimal locomotion in birds and fish [16]. We demonstrate that this optimum results from specific structures present in the wake of the bat and that these occur at high flapping speeds due to the highly three-dimensional nature of bat kinematics. Indeed, when replicating the

simulations under symmetric-flapping kinematics, we find that the optimum shifts to the classical $St \sim 0.3$. This implies that the high Strouhal number of our model results from the specialized kinematics, not the material flexibility.

Finally, we show that reducing membrane stiffness benefits propulsive efficiency. However, for very compliant (i.e small Ca) linear isotropic membranes, we observe membrane flutter and a severe deterioration of the efficiencies. As a result, a strong inverse correlation ($\rho_{\mathcal{E},\eta} = -0.976$) between mean flow enstrophy (mixing) and propulsive efficiency is found. This suggests that membrane wings made of linear isotropic elastic materials are most efficient just before the onset of flutter, which we estimate to occur around $Ca \sim 0.1$. By reinforcing the isotropic membranes with fibres, which capture the response of actual bat skin more accurately, flutter is delayed and high aerodynamic efficiencies can be maintained for $Ca < 0.1$. This effect is similar to an increase in membrane stiffness but without the resulting increase in skin thickness and wing mass, which is likely to have a positive influence on the cost of flight [13], and the nonlinear effect is more pronounced when the loading on the membrane is large, i.e. for high-speed flight. This suggests that the complex fibre arrangement in the bat wing's membrane has evolved to optimize the structural response of the wing by limiting flutter even when flying quickly, ultimately improving its propulsive performance.

4. Methods

4.1. Bat flight kinematics

A parametric model for the wing's motion lets us freely prescribe the bat Strouhal number. Five-degree-of-freedom motion is imposed at the carpus and the rest of the wing passively deforms under aerodynamic and inertial loading. Our parametric kinematic model closely matches experimental measurements, see figure 2*d*, capturing key features of bat flapping such as the angled downstroke plane and the biased power and recovery strokes.

The parametrized flight kinematics is expressed in a fixed Cartesian or global coordinate system ($OXYZ$) and describes the motion and orientation of the carpus ($oxyz$) coordinate system; see figure 2*b*.

The time-dependent angles and translation applied to the carpus are given by

$$\left.\begin{aligned} \mathcal{X}(t) &= A_{\mathcal{X}} \sin(2\pi f t), \\ \mathcal{Y}(t) &= A_{\mathcal{Y}}(\cos(2\pi f t) - 1), \\ \mathcal{Z}(t) &= A_{\mathcal{Z}} \sin(2\pi f t), \\ \theta(t) &= A_\theta(c_1 \cos(2\pi f t + c_2) + (1 - c_1)) \\ \text{and} \quad \phi(t) &= A_\phi \sin(2\pi f t), \end{aligned}\right\} \tag{4.1}$$

where $\mathcal{X}(t)$ is the surge, $\mathcal{Y}(t)$ the sway, $\mathcal{Z}(t)$ the heave, $\theta(t)$ the pitch and $\phi(t)$ the roll. Pitch and roll are rotations around the Y-axis and X-axis, respectively. The non-dimensional amplitudes are $A_{\mathcal{X}}/b = A_{\mathcal{Y}}/b = 0.10$ and $A_{\mathcal{X}}/b = 0.15$, where b is the wing span. These motion amplitudes have been derived from a fit of motion of the wing such that the stroke plane angle is approximately 60° from the horizontal, typical of medium speed flight of bats [4] for a *Glossophaga soricina*, or Palla's long-tongued bat. The roll amplitude is $A_\phi = 30°$, taken from the mean stroke amplitude in [10]. Other authors have reported similar kinematics [4]; see figure 2. The contraction/extension of the wing span during the downstroke/upstroke, resulting from the variation of the $\mathcal{Y}$ position of the carpus, is $A_{\mathcal{Y}}/b \sim 10\%$.

4.1.1. Optimal pitch profile

The effective angle of attack measures the angle between the flow and the wing at the 3/4 chord, $\alpha_{3/4}$, during motion and includes a dynamic upwash correction. For more details, the reader is referred to Izraelevitz *et al.* [28]. To model the different flow conditions along the span, we apply a strip-theory approach, where the wing is discretized in 10 spanwise strips of equal width. For each strip, we compute the effective angle of attack of a point located at 3/4 chord in the middle of the span of the strip. The total effective angle of attack of the wing is found by an area-weighed average of the different strips.

Although this method cannot accurately predict the forces during a cycle, it allows us to estimate the effective angle of attack seen by the wing during a cycle. We can now optimize our analytic form for $\theta(t)$ given by equation (4.1) to achieve the target angle of attack profile $\tilde{\alpha}_{3/4}$ by minimizing a constrained equation of the form

$$A_\theta, c_1, c_2 \rightarrow \underset{A_\theta,\, c_1,\, c_2 \in \mathbb{R}}{\text{minimize}} \ \|\alpha_{3/4}(A_\theta, c_1, c_2) - \tilde{\alpha}_{3/4}\|_2 \tag{4.2}$$

with $A_\theta \in [0, \pi/2]$, $c_1 \in [0.5, 1]$ and $c_2 \in [-\pi/2, \pi/2]$. We use a simple form for the target effective angle of attack, where the upstroke effective angle of attack must vanish and reach target value $\alpha_{\max}$ during the downstroke:

$$\tilde{\alpha}_{3/4} = \begin{cases} \alpha_{\max} & \text{if } \frac{t}{T} > 0.5, \\ 0 & \text{else.} \end{cases} \tag{4.3}$$

We set $\alpha_{\max} = 20$, a common mean effective angle of attack during downstroke [39]. The minimization procedure is carried out for each Strouhal number and results in various amplitudes A_θ, but the other two values were constantly around $c_1 \sim 0.8$ and $c_2 \sim -\pi/8$. Therefore, we fixed those values and repeated the optimization for A_θ only, resulting in $A_\theta = [0.28, 0.45, 0.63, 0.80, 0.98]$ radians for $St = [0.3, 0.4, 0.5, 0.6, 0.7]$, respectively. Sample results of the optimization are presented in electronic supplementary material, Appendix figure S2, showing that this method generates roughly constant lift during the downstroke and very small lift in the upstroke, consistent with actual bat flight [9].

4.2. Hyperelastic formulation

To investigate the effect of membrane compliance and fibre reinforcement on flight efficiency, we use two constitutive models for the membrane: a linear isotropic elastic model and a hyperelastic fibre-reinforced model calibrated on experimentally obtained bat wing membrane properties [18,31]; see figure 2*c*. The fibre-reinforced model introduces microstructural and loading-induced anisotropy in the response of the membrane via a deformation invariant-based hyperelastic strain energy density function [40]. This type of constitutive approach is suited to model a wide class of fibrous biological soft tissues [41–43], including bat wing membrane [31].

Bones in the handwing are more flexible than the humerus and radius and are orders of magnitude stiffer than the membrane they support. In this work, we model the digits with an isotropic material whose Cauchy number is 3000 times larger than the stiffest membrane (i.e. $Ca = 5$), making it effectively highly rigid compared to the membrane. Additionally, the Cauchy scaling using U_{ref} ensures that the bone's deformation is constant (and minimal) across Strouhal numbers. The camber in the find is thus only generated by the deformation of the wing's membrane. Digits typically have thicknesses much greater than the membrane they support. Our simplified model uses a uniform thickness throughout the whole wing and scales the bone's stiffness and density accordingly. To model the fibre-reinforced membrane of the wing, we use a constitutive model based on the strain energy density function

proposed by Holzapfel *et al.* [40] and Gasser *et al.* [44]:

$$\psi = c_e(\bar{I}_1 - 3) + \frac{1}{D}\left(\frac{J^2-1}{2} - \ln J\right) + \sum_{i=4,6} \frac{k_{1,i}}{2k_{2,i}}[\exp(k_{2,i}[\bar{I}_i - 1]^2) - 1], \quad (4.4)$$

where c_e is a material constant related to the matrix shear modulus μ by $c_e = \mu/2$ and D is a material parameter related to the matrix compressibility, or the bulk modulus $K = 2/D$. $\bar{I}_1$ is the first invariant of the isochoric right Cauchy–Green deformation tensor $\overline{\boldsymbol{C}} = \overline{\boldsymbol{F}}^{\top}\overline{\boldsymbol{F}}$, with $\overline{\boldsymbol{F}}$ the isochoric part of the deformation gradient $\boldsymbol{F}$ calculated as $\overline{\boldsymbol{F}} = J^{-1/3}\boldsymbol{F}$, where J is the Jacobian or determinant of the deformation gradient $\boldsymbol{F}$. The anisotropic response of the fibre is introduced through the undeformed mean fibre vector $\mathbf{a}_i$ and the pseudo-invariant of $\bar{I}_i = \boldsymbol{a}_i \cdot (\overline{\boldsymbol{C}}\boldsymbol{a}_i)$, $i = 4$, 6, and represents the stretch along each fibre direction (in this case we have two fibre families, denoted by their invariant-associated index, 4 and 6). $k_{2,i}$ is a dimensionless positive parameter controlling the shape of the nonlinear stiffening of the fibres' mechanical response, and $k_{1,i}$ is an elastic modulus-like parameter corresponding to fibre stiffness. The constitutive parameters of this model are obtained by numerical identification from experimentally measured bat wing membrane properties [18].

The membrane material was assumed to be relatively incompressible by setting the compressibility parameter $D = 20c_e$, leading to an equivalent ground state Poisson's ratio $\nu = 0.475$. The 20 ratio of bulk to shear properties was sufficiently small to prevent numerical ill-conditioning associated with volumetric locking in purely displacement-based finite-element formulations [45] while also ensuring low compressibility.

4.2.1. Hyperelastic calibration

To identify the constitutive parameters in equation (4.4), we fit the experimental data from Skulborstad *et al.* [18] and Skulborstad & Goulbourne [31] to the stress–strain curves from the model in (4.4) under the same equibiaxial loading.

The coefficients $[c_e, k_{1,4}, k_{2,4}, k_{1,6}, k_{2,6}]$ are determined by a L_2-norm minimization of the difference in the stress–strain curves σ_{ii} and the experimental stress/strain curve $\tilde{\sigma}_{ii}$:

$$c_e, k_{1,4}, k_{2,4}, k_{1,6}, k_{2,6} \rightarrow \underbrace{\text{minimize}}_{c_e,k_{1,4},k_{2,4},k_{1,6},k_{2,6}\in\mathbb{R}^+} \|\sigma_{ii} - \tilde{\sigma}_{ii}\|_2. \quad (4.5)$$

In practice, we find that c_e tends to take negative values; as this would result in unphysical material behaviour, we fix its value to $c_e = 20$. The different parameters found are $k_{1,4} = 33.5$, $k_{2,4} = 13.5$, $k_{1,6} = 102.7$, $k_{2,6} = 12.3$.

These coefficients can then be injected into the numerical model for the bat wing; the difficulty lies in scaling the fitted parameters into a dimensionless form employed in our numerical simulation. To scale the fitted hyperelastic parameters and compare fibre-reinforced membranes with isotropic membranes, we must be able to express both in terms of Ca. For a linear isotropic elastic constitutive law, E is readily available (and constant). For the transversely isotropic hyperelastic fibre-reinforced membrane, E is a function of the deformation (through $\overline{\boldsymbol{C}}$), making a simple estimate unavailable. To alleviate this problem, we use an initial tangent stiffness modulus approach to estimate the initial stiffness of the hyperelastic material (in the limit of vanishing strain); see figure 2*c*. This tangent stiffness modulus approach ensures that linear isotropic and nonlinear fibre-reinforced membranes behave similarly in the small strain limit and ultimately allow us to compare them. Finally, we use equation (2.1) to express the different material coefficients at different Cauchy numbers.

Table 1. Convergence of aerodynamic force coefficients of the bat wing simulations for a Strouhal number $St = 0.5$ and $Ca = 0.5$ using an isotropic linear elastic membrane for various resolutions.

N_x	$\overline{C_T}$	$\overline{C_L}$	$\overline{C_{Pow}}$	η_p (%)
32	0.0520	0.2179	0.1626	31.97
64	0.0880	0.2013	0.2069	42.52
96	0.0975	0.1881	0.2174	44.84
128	0.0998	0.1914	0.2204	45.28

4.3. Numerical setup

We perform all the simulations with our validated fluid–structure interaction solver [29,30] which couples an immersed boundary finite volume method for the fluid with a shell finite-element method for the structure. Defining b as the handwing span, the fluid domain consists of a uniform region of dimensions $[2.5, 1.2, 1.2] \times b$, centred around the wing. Grid stretching fills the domain until it reaches a total size of $[12, 6, 6] \times b$. Because of the symmetry of the problem, we only model the bat's right wing and apply a symmetry boundary condition on the centreline of the domain (i.e. the middle of the bat's body) to reduce the computational load. A uniform free-stream velocity U is imposed on the inlet of the fluid domain, while a zero pressure gradient condition is used on the outlet. The no-slip condition is applied to the immersed wing, and all other fluid domain boundaries are threaded as free-slip walls. The wing is modelled as an initially flat shell with constant thickness $h/b = 0.005$ and the fixed-point fluid–structure interaction problem is solved using a quasi-Newton scheme until the relative residuals between consecutive coupling iterations drop below 10^{-4} for both the displacements and the forces [30]. This typically takes two iterations per time step, as the mass ratio of the simulations is relatively large (small added-mass effects). In our simulations, the flow evolves for six cycles. However, we found excellent repeatability after two cycles and we phase-average the quantities of interest over the last four cycles. The cycle-averaged values are then obtained by averaging the phase-averaged data.

Table 1 shows the results of a mesh convergence study for a Strouhal number $St = 0.5$ and a Cauchy number $Ca = 0.5$. We vary the mesh resolution $N_x = b/\Delta x \in [32, 64, 96, 128]$. We compare the cycle-averaged force coefficients to the finest mesh and find that reducing the resolution toward $N_x = 128$ changes the resulting forces by approximately 1%. We use the $N_x = 96$ mesh for all the simulations presented herein, giving a non-dimensional wall distance $y^+ \sim 5$, assuming a flat plate 1/7 power law for the velocity profile. The total fluid mesh count is around 12.8M control volumes. For the structural model, 64 linear triangular elements along each digit, giving a total mesh count of 13 093 elements.

Simulations were performed on the *Iridis 5* supercomputer at the University of Southampton. Typical simulations used 64 2.0-GHz Intel Skylake processors for the fluid domain and 4 for the structural problem. Simulations took 3–4 days to reach six motion cycles (at $St = 0.5$) at this resolution with a fixed time step $\Delta t U/\Delta x = 0.2$.

Ethics. This work did not require ethical approval from a human subject or animal welfare committee.

Data accessibility. The data generated for this study and the scripts to perform the analysis are available from the Biorxiv archive: https://www.biorxiv.org/content/10.1101/2023.09.11.557136v2 [46].

Supplementary material is available online [47].

Declaration of AI use. We have not used AI-assisted technologies in creating this article.

Authors' contributions. M.L.: conceptualization, data curation, formal analysis, investigation, methodology, software, validation, visualization, writing—original draft, writing—review and editing; G.D.W.: conceptualization, funding acquisition, investigation, methodology, project administration, resources, supervision, writing—review and editing; G.L.: conceptualization, funding acquisition, investigation, methodology, project administration, resources, supervision, writing—review and editing.

All authors gave final approval for publication and agreed to be held accountable for the work performed therein.

Conflict of interest declaration. We declare we have no competing interests.

Funding. This work was financially supported by UK Research and Innovation grant no. EP/L015382/1.

Acknowledgements. We would like to thank Kenny S. Breuer for comments on an early version of the manuscript.

References

1. Swartz SM, Konow N. 2015 Advances in the study of bat flight: the wing and the wind. *Can. J. Zool.* **93**, 977–990. (doi:10.1139/cjz-2015-0117)
2. Norberg UM. 1976 Aerodynamics, kinematics and energetics of horizontal flapping flight in the long-eared bat *Plecotus auritus*. *J. Exp. Biol.* **65**, 179–212. (doi:10.1242/jeb.65.1.179)
3. Aldridge HD. 1986 Kinematics and aerodynamics of the greater horseshoe bat, *Rhinolophus ferrumequinum*, in horizontal flight at various speeds. *J. Exp. Biol.* **126**, 479–497. (doi:10.1242/jeb.126.1.479)
4. Wolf M, Johansson LC, Von Busse R, Winter Y, Hedenström A. 2010 Kinematics of flight and the relationship to the vortex wake of a Pallas' long tongued bat (*Glossophaga soricina*). *J. Exp. Biol.* **213**, 2142–2153. (doi:10.1242/jeb.029777)
5. Von Busse R, Hedenström A, Winter Y, Johansson LC. 2012 Kinematics and wing shape across flight speed in the bat, *Leptonycteris yerbabuenae*. *Biol. Open* **1**, 1226–1238. (doi:10.1242/bio.20122964)
6. Bahlman JW, Swartz SM, Breuer KS. 2014 How wing kinematics affect power requirements and aerodynamic force production in a robotic bat wing. *Bioinspir. Biomim.* **9**, 025008. (doi:10.1088/1748-3182/9/2/025008)
7. Viswanath K, Nagendra K, Cotter J, Frauenthal M, Tafti DK. 2014 Straight-line climbing flight aerodynamics of a fruit bat. *Phys. Fluids* **26**, 021901. (doi:10.1063/1.4864297)
8. Swartz SM, Iriarte-Díaz J, Riskin DK, Breuer KS. 2012 A bird? A plane? No, it's a bat: an introduction to the biomechanics of bat flight. *Evol. Hist. Bats: Foss. Mol. Morphol.* **1**, 317–352. (doi:10.1017/CBO9781139045599.010)
9. Hedenström A, Johansson LC. 2015 Bat flight. *Curr. Biol.* **25**, 399–402. (doi:10.1016/J.CUB.2015.04.002)
10. Bullen RD, McKenzie NL. 2002 Scaling bat wingbeat frequency and amplitude. *J. Exp. Biol.* **205**, 2615–2626. (doi:10.1242/jeb.205.17.2615)
11. Cheney JA, Konow N, Bearnot A, Swartz SM. 2015 A wrinkle in flight: the role of elastin fibres in the mechanical behaviour of bat wing membranes. *J. R. Soc. Interface* **12**, 20141286. (doi:10.1098/RSIF.2014.1286)
12. Wang S, Zhang X, He G, Liu T. 2015 Lift enhancement by bats' dynamically changing wingspan. *J. R. Soc. Interface* **12**, 20150821. (doi:10.1098/RSIF.2015.0821)
13. Riskin DK, Bergou A, Breuer KS, Swartz SM. 2012 Upstroke wing flexion and the inertial cost of bat flight. *Proc. R. Soc. B* **279**, 2945–2950. (doi:10.1098/RSPB.2012.0346)
14. Fan X, Swartz S, Breuer K. 2022 Power requirements for bat-inspired flapping flight with heavy, highly articulated and cambered wings. *J. R. Soc. Interface* **19**, 20220315. (doi:10.1098/RSIF.2022.0315)
15. Pennycuick CJ. 1996 Wingbeat frequency of birds in steady cruising flight: new data and improved predictions. *J. Exp. Biol.* **199**, 1613–1618. (doi:10.1242/jeb.199.7.1613)
16. Taylor GK, Nudds RL, Thomas ALR. 2003 Flying and swimming animals cruise at a Strouhal number tuned for high power efficiency. *Nature* **425**, 707–711. (doi:10.1002/jmor.1051430305)
17. Swartz SM, Groves MS, Kim HD, Walsh WR. 1996 Mechanical properties of bat wing membrane skin. *J. Zool.* **239**, 357–378. (doi:10.1111/j.1469-7998.1996.tb05455.x)
18. Skulborstad AJ, Swartz SM, Goulbourne NC. 2015 Biaxial mechanical characterization of bat wing skin. *Bioinspir. Biomim.* **10**, 036004. (doi:10.1088/1748-3190/10/3/036004)
19. Holbrook KA, Odland GF. 1978 A collagen and elastic network in the wing of the bat. *J. Anat.* **126**, 21–36.
20. Cheney JA, Rehm JC, Swartz SM, Breuer KS. 2022 Bats actively modulate membrane compliance to control camber and reduce drag. *J. Exp. Biol.* **225**, jeb243974. (doi:10.1242/jeb.243974)
21. Wang S, Zhang X, He G, Liu T. 2015 Numerical simulation of unsteady flows over a slow-flying bat. *Theor. Appl. Mech. Lett.* **5**, 5–8. (doi:10.1016/J.TAML.2015.01.006)
22. Li G, Law YZ, Jaiman RK. 2019 A novel 3D variational aeroelastic framework for flexible multibody dynamics: application to bat-like flapping dynamics. *Comput. Fluids* **180**, 96–116. (doi:10.1016/j.compfluid.2018.11.013)
23. Joshi V, Jaiman R, Li G, Breuer KS, Swartz SM. 2020 Full-scale aeroelastic simulations of hovering bat flight. *AIAA Scitech 2020 Forum* **1**, 1–19. (doi:10.2514/6.2020-0335)
24. Lin YL, Derr NJ, Rycroft CH. 2021 Eulerian simulation of complex suspensions and biolocomotion in three dimensions. *Proc. Natl Acad. Sci. USA* **119**, e2105338118. (doi:10.1073/pnas.2105338118)
25. Hu HZ, Wang J, Wang Y, Dong H. 2021 Effects of tunable stiffness on the hydrodynamics and flow features of a passive pitching panel. *J. Fluids Struct.* **100**, 2020103175. (doi:10.1016/j.jfluidstructs.2020.103175)
26. Zurman-Nasution AN, Weymouth GD, Ganapathisubramani B. 2021 Fin sweep angle does not determine flapping propulsive performance. *J. R. Soc. Interface* **18**, 20210174. (doi:10.1098/rsif.2021.0174)
27. Theodorsen T. 1935 General theory of aerodynamic instability and the mechanism of flutter. *Annu. Rep. Natl Advis. Comm. Aeronaut.* **268**, 413.
28. Izraelevitz JS, Kotidis M, Triantafyllou MS. 2018 Optimized kinematics enable both aerial and aquatic propulsion from a single three-dimensional flapping wing. *Phys. Rev. Fluids* **3**, 073102. (doi:10.1103/PhysRevFluids.3.073102)
29. Lauber M, Weymouth GD, Limbert G. 2022 Immersed boundary simulations of flows driven by moving thin membranes. *J. Comput. Phys.* **457**, 111076. (doi:10.1016/J.JCP.2022.111076)
30. Lauber M, Weymouth GD, Limbert G. 2023 Immersed-boundary fluid-structure interaction of shells and membranes. In *Proc. XII Int. Conf. on Structural Dynamics (EURODYN), Delft, The Netherlands, 2–5 July 2023*.
31. Skulborstad AJ, Goulbourne NC. 2014 Structurally motivated constitutive model for bat wing skin. *Proc. ASME 2014 Int. Mechanical Engineering Congress and Exposition* **9**, V009T12A091. (doi:10.1115/IMECE2014-39525)
32. Eldredge JD, Jones AR. 2019 Leading-edge vortices: mechanics and modeling. *Annu. Rev. Fluid Mech.* **51**, 75–104. (doi:10.1146/annurev-fluid-010518)
33. Johansson LC, Håkansson J, Jakobsen L, Hedenström A. 2016 Ear-body lift and a novel thrust generating mechanism revealed by the complex wake of brown long-eared bats (*Plecotus auritus*). *Sci. Rep.* **6**, 24886. (doi:10.1038/srep24886)
34. Engels T, Wehmann HN, Lehmann FO. 2020 Three-dimensional wing structure attenuates aerodynamic efficiency in flapping fly wings. *J. R. Soc. Interface* **17**, 20190804. (doi:10.1098/RSIF.2019.0804)
35. Dong H, Mittal R, Najjar FM. 2006 Wake topology and hydrodynamic performance of low-aspect-ratio flapping foils. *J. Fluid Mech.* **566**, 309–343. (doi:10.1017/S002211200600190X)
36. Vianello M. 1996 Optimization of the stored energy and coaxiality of strain and stress in finite elasticity. *J. Elast.* **44**, 193. (doi:10.1007/BF00042131)
37. Menzel A. 2005 Modelling of anisotropic growth in biological tissues: a new approach and computational aspects. *Biomech. Model. Mechanobiol.* **3**, 147–171. (doi:10.1007/s10237-004-0047-6)

38. Kuhl E, Holzapfel GA. 2007 A continuum model for remodeling in living structures. *J. Mater. Sci.* **42**, 8811–8823. (doi:10.1007/s10853-007-1917-y)
39. Chen L, Yang FL, Wang YQ. 2022 Analysis of nonlinear aerodynamic performance and passive deformation of a flexible flapping wing in hover flight. *J. Fluids Struct.* **108**, 2021103458. (doi:10.1016/j.jfluidstructs.2021.103458)
40. Holzapfel GA, Gasser TC, Ogden RW. 2000 A new constitutive framework for arterial wall mechanics and a comparative study of material models. *J. Elast.* **61**, 1–48. (doi:10.1023/A:1010835316564)
41. Limbert G, Taylor M. 2002 On the constitutive modeling of biological soft connective tissues: a general theoretical framework and explicit forms of the tensors of elasticity for strongly anisotropic continuum fiber-reinforced composites at finite strain. *Int. J. Solids Struct.* **39**, 2343–2358. (doi:10.1016/S0020-7683(02)00084-7)
42. Humphrey JD. 2003 Continuum biomechanics of soft biological tissues. *Proc. R. Soc. Lond. A* **459**, 3–46. (doi:10.1098/rspa.2002.1060)
43. Limbert G. 2017 Mathematical and computational modelling of skin biophysics: a review. *Proc. R. Soc. A* **473**, 20170257. (doi:10.1098/rspa.2017.0257)
44. Gasser TC, Ogden RW, Holzapfel GA. 2006 Hyperelastic modelling of arterial layers with distributed collagen fibre orientations. *J. R. Soc. Interface* **3**, 15–35. (doi:10.1098/rsif.2005.0073)
45. Simo JC, Taylor RL. 1991 Quasi-incompressible finite elasticity in principal stretches continuum basis and numerical algorithms. *Comput. Methods Appl. Mech. Eng.* **85**, 273–310. (doi:10.1016/0045-7825(91)90100-K)
46. Lauber M, Weymouth GD, Limbert G. 2023 Data from: Rapid flapping and fiber-reinforced membrane wings are key to high-performance bat flight. Biorxiv. (https://www.biorxiv.org/content/10.1101/2023.09.11.557136v2)
47. Lauber M, Weymouth GD, Limbert G. 2023 Rapid flapping and fiber-reinforced membrane wings are key to high-performance bat flight. Figshare. (doi:10.6084/m9.figshare.c.6916153)